Article:
Ren, K., Hu, J., Bi, C. et al. (6 more authors) (2024) Strongly-Confined CsPbI3 Quantum Dots by Surface Cleaning-Induced Ligand Exchange for Spectrally Stable Pure-Red Light-Emitting Diodes with Efficiency Exceeding 26%. ACS Materials Letters, 6. pp. 4115-4123. ISSN 2639-4979

https://doi.org/10.1021/acsmaterialslett.4c00912

Supporting Information

Strongly-Confined $CsPbI_3$ Quantum Dots by Surface Cleaning-Induced Ligand Exchange for Spectrally Stable Pure-Red Light-Emitting Diodes with Efficiency Exceeding 26%

Ke Ren[1,2†], Jingcong Hu[4†], Chenghao Bi[1,2,3†*], Shibo Wei[1,2], Xingyu Wang[5,6], Nora H. de Leeuw[5,6], Yue Lu[4*], Manling Sui[4*], Wenxin Wang[1,2*]

[1] Qingdao Innovation and Development Base, Harbin Engineering University, Qingdao 266000, P. R. China.

[2] College of Physics and Optoelectronic Engineering, Harbin Engineering University, Harbin 150001, P. R. China.

[3] Yantai Research Institute, Harbin Engineering University, Yantai 264000, P.R. China.

[4] Beijing Key Lab of Microstructure and Property of Advanced Materials, College of Materials Science and Engineering, Beijing University of Technology, Beijing 100124, P. R. China.

[5] School of Chemistry, University of Leeds, Leeds LS2 9JT, UK.

[6] Department of Earth Sciences, Utrecht University, 3584 CB Utrecht, The Netherlands.

†These authors contributed equally to this work.

E-mail: chenghao.bi@hrbeu.edu.cn; luyue@bjut.edu.cn; mlsui@bjut.edu.cn; wenxin.wang@hrbeu.edu.cn

Experimental Section

Materials

3-phenyl-1-propylamine (3-PA, Aladdin, 98%), zinc iodide (ZnI_2, Aladdin, 99.99%), octadecene (ODE, Sigma-Aldrich, 90%), cesium carbonate (Cs_2CO_3, Alfa-Aesar, 99.9%), lead iodide (PbI_2, Advanced Election Technology Co.,Ltd, 99.9%), lead bromide ($PbBr_2$, Advanced Election Technology Co.,Ltd, 99.9%), 1,3,5-Tris(1-phenyl-1H-benzimidazol-2-yl)benzene (TPBi, Advanced Election Technology Co.,Ltd, 99%), tetrabutylammonium iodide (TBAI, Aladdin, 95%), oleic acid (OA, Alfa-Aesar, 90%), oleylamine (OAm, Aladdin, 90%), n-hexane (Aladdin, 99%), n-octane (Maclean's, 95%), and methyl acetate (Aladdin, 99%), and hydrogen bromide (HBr, Ballantine's, 33% acetic acid solution), which are used directly.

Preparation of cesium oleate precursor

In a 50 mL three-necked flask, the 10 mL of ODE is mixed with 100 mg of Cs_2CO_3 and 700 μL of OA and stirred in vacuo at 100 °C for 1 h and then kept at temperature until the Cs_2CO_3 is completely dissolved. Then nitrogen is pumped into the flask and degassed for 20 min. The process is repeated three times to obtain the cesium-oleic acid solution that completely remove H_2O and O_2. The cesium-oleic acid solution is maintained at about 100 °C until used for the synthesis of QDs.

Preparation and purification of mix-halide $CsPbBr_xI_{3-x}$ QDs (QDs-M)

QDs-M are prepared here by thermal injection. The 10 mL of ODE, 124 mg of PbI_2 and 4 mg of $PbBr_2$ are mixed into a 100 mL oblique three-necked flask and stirred for 1 h at 120 °C under vacuum. The mixture is then charged sequentially with 1 mL of OA and OAm solution. The temperature is raised to 170 - 175 °C under nitrogen. 1.6 mL of cesium-oleate solution is injected into it after the solutes in the mixture are completely dissolved. Then we quickly transfer the flask to an ice-water bath. After cooling to room temperature, the mixture is transferred to a 100 mL centrifuge tube. 30 - 60 mL of methyl acetate is added to the tube and centrifuged at 8000 rpm for 5 min. The precipitate is taken from the centrifuge tube and dispensed in 1 mL of n-octane, which is prepared for the PeLED fabrication.

Preparation and purification of strongly-confined $CsPbI_3$ QDs (SQDs)

Here, SQDs are prepared by thermal injection. The 10 mL of ODE, 173 mg of PbI_2 and 360 mg of ZnI_2 are mixed into a 100 mL oblique three-necked flask. The temperature of the mixed solution slowly rose to 120 °C within 1 h under vacuum. Then 3 mL of OA/OAm mixture is sequentially injected into the mixture and the temperature is raised to 170 - 175 °C under nitrogen. When the solutes in the mixture are completely dissolved, 1.6 mL of cesium-oleate solution is injected into it. We then quickly transfer the flask to an ice-water bath. After cooling to room temperature, the mixture is transferred to a 100 mL centrifuge tube. 10 - 20 mL of methyl acetate is added to the tube and centrifuged at 8000 rpm for 5 min. After the supernatant is taken, 20 - 30 mL methyl acetate is added and centrifuged at 8000 rpm for 5 min. Take the precipitate from the centrifuge tube and redisperse it with 1 mL of the n-hexane to obtain the SQDs.

Preparation and purification of surface-cleaning $CsPbI_3$ QDs (SQDs-H)

The method of synthesizing SQDs-H is basically the same as that of SQDs. It is also need to mix 10 mL of ODE, 173 mg of PbI_2 and 360 mg of ZnI_2 into a 100 mL oblique three-necked flask.

After the mixed solution is cooled to room temperature by an ice-water bath, the mixture is again warmed to 60 °C and 60 μL of HBr solution is injected into it. After fully stirring, the mixture is transferred to a 100 mL centrifuge tube. Then the SQDs-H are purified by methyl acetate. The precipitate from the centrifuge tube is re-dispersed with 1 mL of n-hexane to obtain the SQDs-H.

Preparation and purification of ligand-exchanged $CsPbI_3$ QDs (SQDs-T)

In addition to ligand exchange, the process of SQDs-T and SQDs-H are consistent. 50 μL of 3-PA solution is added after 10 s of HBr injection. Then the inclined three-necked flask is transferred again to the ice-water bath for rapid cooling. During this period, the mixed solution in the oblique three-necked flask is still stirred continuously.

Characterization of $CsPbI_3$ QDs

Transmission electron microscopy (TEM) and high-resolution (HR) TEM images are done on a JEM-2100 (JEOL) at 200 kV, and a Titan G2 60-300 Cs corrected TEM operated at 300 kV, the energy resolution of EDS is 137 eV. X-ray diffraction (XRD) is obtained using Cu Kα radiation (λ = 1.5418 Å) on an X-ray diffractometer (Bruker, D8 Focus). Steady-state ultraviolet-visible (UV-vis) absorption is measured using a Perkin Elmer Lambda 1050+ UV spectrophotometer. Steady-state PL emission is measured by an F-380 spectrometer. An Oxford Instruments Optistat-DN is used to acquire temperature-dependent PL spectra in the range 80 - 220 K. All the PLQY data is collected based QDs solution. PLQY of QDs solutions is acquired by an integrating sphere (Edinburgh, FLS920) with an excitation wavelength of 530 nm. Time-resolved PL decays are recorded on a Horiba Fluor log spectrometer with a 375 nm, 45 ps pulsed laser and a time-corrected single photon counting system. Concentration decay curves are fitted by a function and the average PL lifetime is calculated according to the standard rule. X-ray photoelectron spectroscopy (XPS) is acquired by a PHI 5000 Versa Probe III spectrometer using a monochromatic AlKα radiation source (1486.6 eV). Electron microscope (FE-SEM, SU4800, Hitachi) to investigate the cross-sectional images of PeLEDs. All measurements are performed at room temperature except for the temperature-dependent PL spectra.

Device Fabrication and Characterization

Firstly, the ITO-coated glasses are ultrasonically cleaned, mainly using a cleaning solution, deionized water, acetone, and ethanol. Each is ultrasound for 30 min. Then, the ITO-coated glasses are dried using dry compressed air. After drying, the glass is placed in UV-ozone cleaner for 30 min. PEDOT:PSS is infiltrated through a 0.22 μm Nylon filter and spin-coated onto ITO-coated glass at a speed of 3500 rpm for 40 seconds. Subsequently, the samples are annealed in air at 140 °C for 10 min. Move the prepared coated substrate into a glove box filled with nitrogen. Poly-TPD is dissolved in chlorobenzene solution (8 mg/mL), and then the solution is uniformly coated on the PEDOT:PSS layer at a speed of 2500 rpm for 40 s. The substrate is then annealed at 130 °C for 25 min. The poly-TPD layer is spin-coated with the $CsPbI_3$ QDs solution for 40 s at a speed of 1000 rpm. For the QDs used in PeLEDs, 1.5 - 3 mL of methyl acetate is added to 1 mL of n-hexane and centrifuged. Then centrifuge at 8000 rpm for 5 min. The separated precipitate is dispersed in 0.5 mL of n-octane and added small amounts of ZnI_2 and TBAI to QDs, which is used to further improve the performance of QDs for subsequent PeLEDs preparation. Using a thermal evaporation technique, a layer of TPBi (40 nm), LiF (1 nm), and Al (100 nm) are successively deposited. The PeLED utilized in the test is not packaged, and all tests are conducted in air at room temperature. A system containing a Keithley

2612 m, PR-670 Spectra Scan spectroradiometer, and Newport 918-D-SL0D3R silicon photodiode is used to get the J-V and L-V curves, EQE, EL spectra, CIE, and operational T_{50} of Pe LEDs.

Computational Method

In this work, all calculations are carried out using the Vienna Ab initio Simulation Package (VASP) with the projector augmented wave (PAW) method. The Perdew-Burke-Ernzerhof (PBE) functional with the generalized gradient approximation (GGA) method is used in combination with the DFT-D3 correction. The cut-off energy of the plane-wave basis is set at 500 eV. A vacuum width of 25 Å is added in all surface models. In the calculations, we have used the Brillouin zone integration with 2×2×1 Gamma-centre k-point sampling. Gaussian smearing of 0.05 eV is used for all calculations. The self-consistent calculations applied a convergence energy threshold of 10^{-5} eV, and the equilibrium geometries are optimized with maximum stress on each atom within 0.03 eV/Å. In our work, atoms in the top half of the surface layers are allowed to relax, while the bottom half layers are fixed to mimic the bulk material during optimization. The adsorption energies are calculated through the following equation:

$$\Delta E_{absorbate}=E_{absorbate}-E_{sur}-E_{molecule};$$

Where $E_{absorbate}$, E_{sur} and $E_{molecule}$ are the total energies of the adsorbate model, pure surface and adsorbed molecules obtained from the DFT simulations, respectively.

Supplementary Notes

Calculation of Urbach energy

The Urbach method is a method for measuring non-radiative leaps at the edges of the energy bands of semiconductor materials. And it is often used to assess the quality of materials and the strength of non-radiative leaps. According to the Urbach method, the optical absorption at the energy band edges can be approximated in an exponential form, which is calculated as:

$$\alpha = \alpha_0 \exp(\frac{h\upsilon - E_0}{E_u});$$

Where α represents the optical absorption at the edge of the energy band, α_0 is a constant, $h\upsilon$ is the energy at the edge of the energy band, E_0 is the energy at the bottom of the conduction band, and E_u is the Urbach Energy, which is used to describe the degree of expansion of the energy band edge.

Calculation of exciton binding energy

Calculating the exciton binding energy from a curve fit to a variable temperature photoluminescence (PL) spectrum is a common method. Typically, the following equation can be used to calculate the exciton binding energy:

$$\frac{1}{I(T)} = \frac{1}{I_0} + \frac{A}{I_0} \exp(-\frac{E_B}{k_B T});$$

Where $I(T)$ is obtained by collecting the normalized integral area of the PL spectrum of the sample at different temperatures. I_0 is the normalized integrated area of the PL spectrum of the sample at 0 K, k_B is the Boltzmann constant, and A is the pre-exponential constant.

The calculations of EQE of PeLEDs

The EQE (External Quantum Efficiency) of the PeLEDs is calculated using the equation:

$$\eta_{EQE} = \frac{C\eta_c \int \lambda I(\lambda) d\lambda}{\int I(\lambda) g(\lambda) d\lambda};$$

Where η_c represents the current efficiency, λ is the wavelength, $I(\lambda)$ is the EL intensity, $g(\lambda)$ is the photonic response of the human eye at a specific wavelength, and C is a constant.

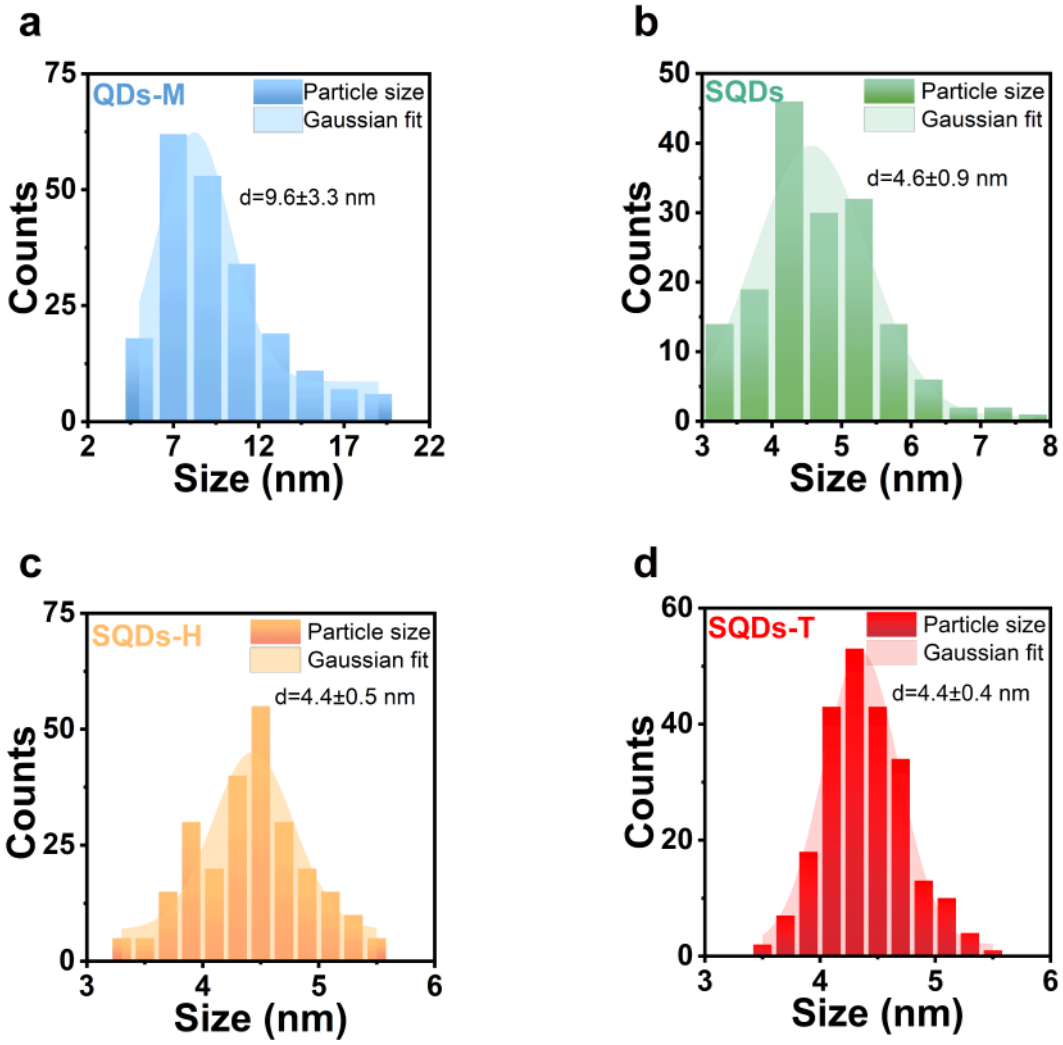

Figure S1. The size distribution histograms of **a** pure-red QDs synthesized by the conventional method (QDs-M), **b** SQDs, **c** SQDs-H, and **d** SQDs-T. The average sizes are calculated assuming that the data approximate Gaussian distributions.

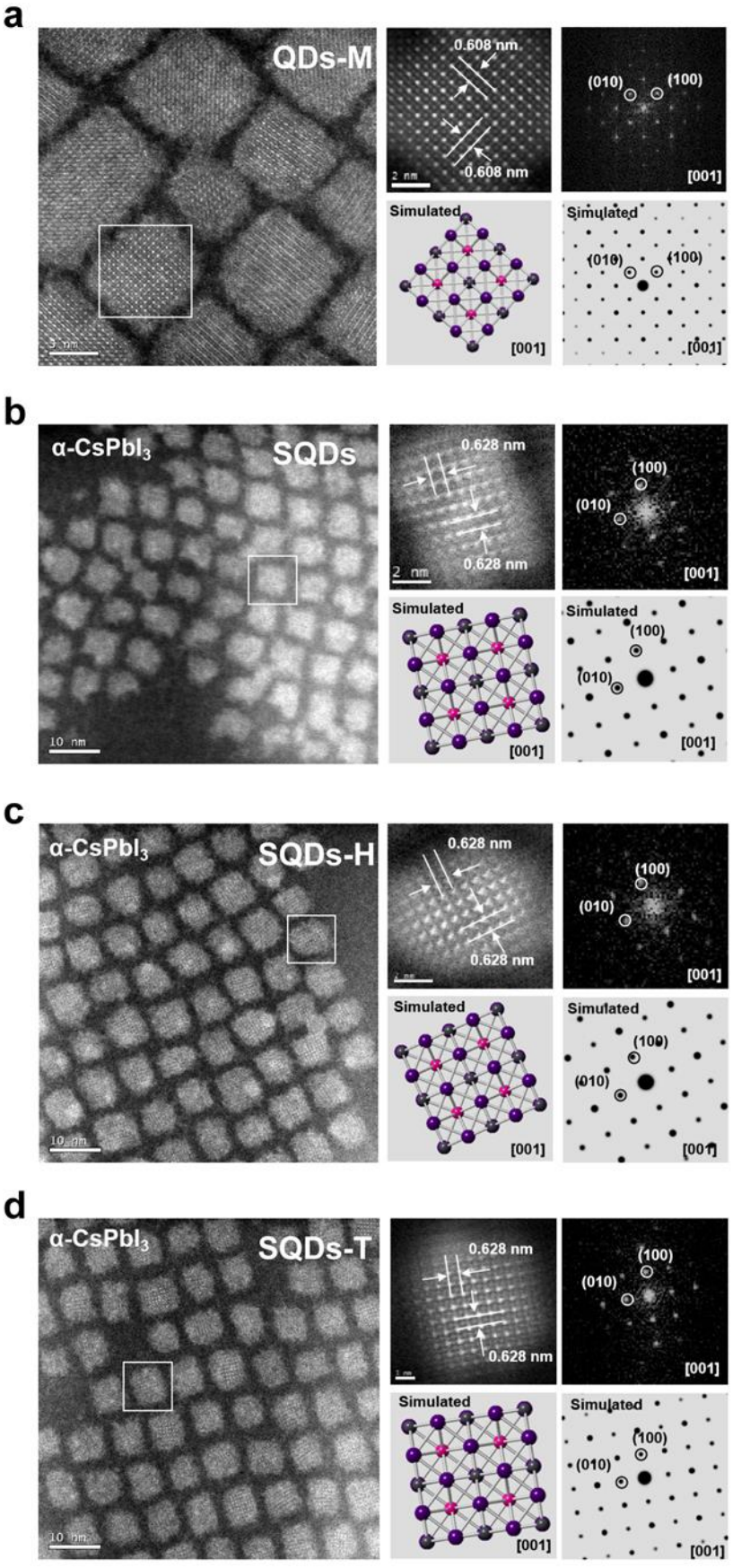

Figure S2. Low magnification and atomic resolution High Angle Annular Dark Field Scanning

Transmission Electron Microscopy (HAADF-STEM) images of four kinds of quantum dots (**a** QDs-M, **b** SQDs, **c** SQDs-H, **d** SQDs-T) are obtained. Corresponding Fast Fourier Transform (FFT) patterns are acquired from selected regions shown in white boxes. Simulated crystal structures and FFT patterns of control quantum dots are also generated.

We observe the lattice spacing of the QDs using high-resolution transmission electron microscopy (HRTEM). The images show that the lattice spacing of SQDs, SQDs-H and SQDs-T are all 0.628 nm. This distance aligns precisely with the (100) crystal plane of the cubic $CsPbI_3$ structure, validating the congruency with the X-ray diffraction (XRD) findings.

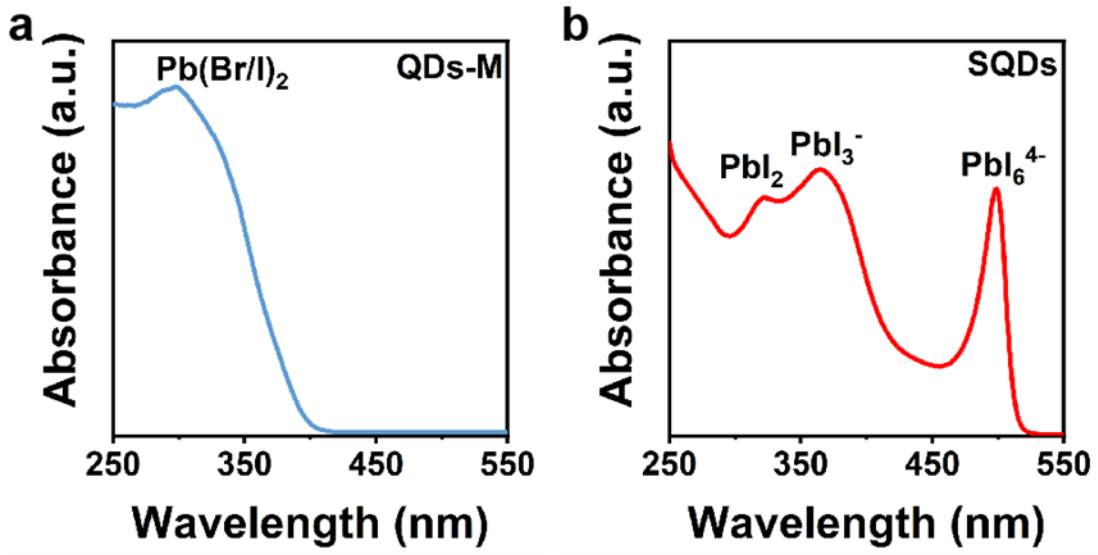

Figure S3. Absorption spectra of **a** QDs-M and **b** SQDs lead precursor solutions in n-octane.

For QDs-M, the Pb-precursor only presents a sharp absorption peak at 300 nm. In general, the absorption peaks are about 320 nm for PbI_2 and 275 nm for $PbBr_2$. The UV-vis spectrum has an absorption peak of 300 nm in the **Figure S3a**, which belongs to the characteristic peak of $Pb(Br/I)_2$. And a new absorption peak at 320 nm, 373 nm and 495 nm can be observed in the high I/Pb ratios precursor, which corresponds to PbI_2, $[PbI_3]^-$ and $[PbI_6]^{4-}$ complexes. This demonstrates that PbI_2 is gradually combined with excess I^- ions to form $[PbI_3]^-$ and $[PbI_6]^{4-}$ complexes for the high I/Pb ratio precursors, which is an indispensable intermediate for the formation of the perovskite monomers. Thus, the perovskite monomer formation step will be shortened due to the formation of $[PbI_3]^-$ and $[PbI_6]^{4-}$ complexes in high I/Pb ratio precursors, leading to an accelerated monomer supply rate, which in turn leads to an accelerated nucleation speed of perovskite QDs. The discussion above demonstrates that the nucleation speed is accelerated in the high I/Pb ratios precursor, thereby achieving narrow size-distribution perovskite QDs.

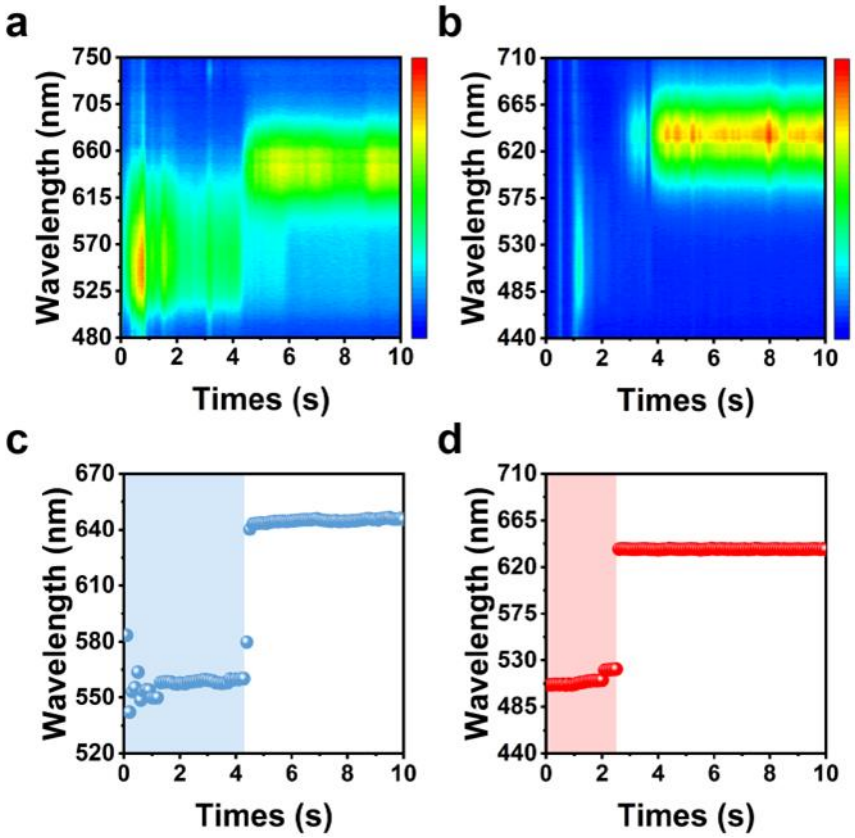

Figure S4. In-situ PL spectra of **a, c** QDs-M and **b, d** SQDs.

We also measure the in-situ PL spectra of the QDs-M and SQDs. For SQDs, after the Cs precursor is injected, a rapid red-shift of the emission wavelength (~ 2 s) is observed firstly and then remains unchanged. On the contrary, the emission wavelength of QDs-M exhibits a red shift with a longer time (~ 4.2 s) and a continuous slow red-shift. This result indicates a faster nucleation and growth process of SQDs, which is related to the formation of $[PbI_6]^{4-}$ complex in the iodide-rich environment.

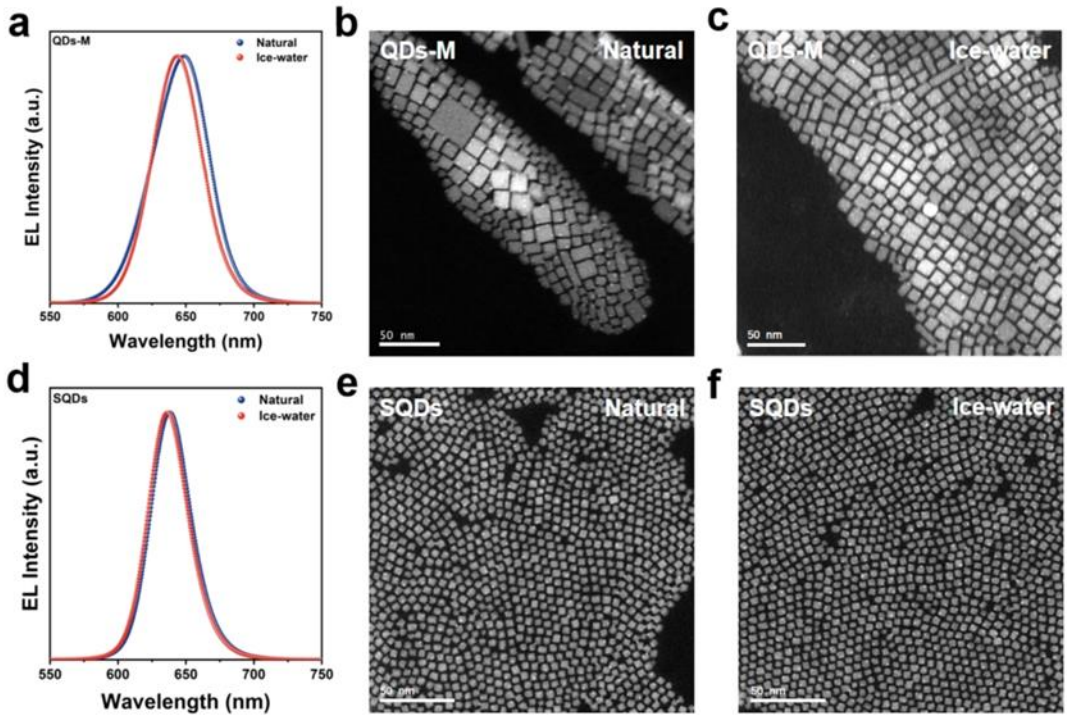

Figure S5. The optical properties and morphological characteristics of SQDs produced by different quenching speeds, **a, d** comparison of PL spectra of QDs-M and SQDs under natural cooling and ice-water cooling, **b, c** TEM of QDs-M under **b** natural cooling and **c** ice-water cooling, TEM of SQDs under **e** natural cooling and **f** ice-water cooling.

In order to provide more evidence of the suppression of the Ostwald ripening process in the SQDs, we conduct a comparison of the optical properties and morphological characteristics of QDs generated through various quenching speeds, including natural cooling and ice-water cooling. **Figure S5a** and **S5d** exhibit the PL spectra of the QDs-M and SQDs acquired through different quenching techniques, respectively. The PL spectra of the QDs-M in the natural cooling area has a significant red shift, and the FWHM is widened. However, the PL spectra of the SQDs obtained through natural cooling exhibit almost no red-shift when contrasts with those obtained through ice-water cooling. Furthermore, the TEM images obtained by the two different cooling methods are significantly different (**Figure S5b, c**). The Ostwald ripening process occurs constantly inside the QDs-M in the natural cooling, and QDs continue to grow, so finally form some nanosheets with super-large size. However, the TEM morphology of SQDs prepared by ice-water and natural cooling is very similar (**Figure S5e, f**). The process of Ostwald ripening is effectively suppressed in the QDs, resulting is nearly identical PL spectra and TEM images of the products acquired through the two distinct quenching methods.

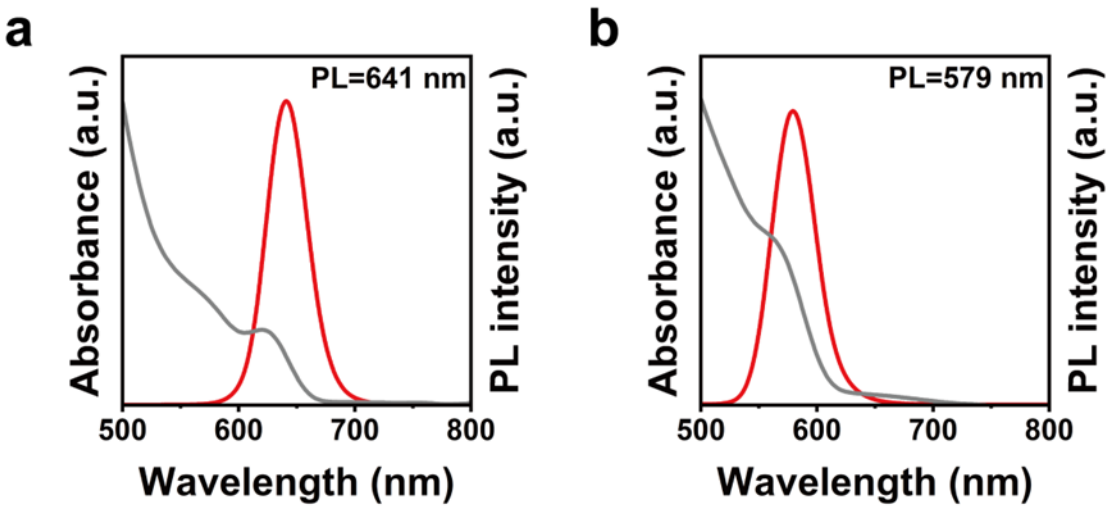

Figure S6. PL and UV-vis spectra of **a** SQDs and **b** SQDs after adding 60 μL HBr.

To verify if there is an ion exchange process between SQDs and HBr, we add 60 μL HBr in SQDs solutions and measure their PL and UV-vis spectra. SQDs adding HBr exhibit an obvious blue-shift of the excitonic peak at 567 nm and PL emission at 579 nm compared with SQDs. It is attributed to the ion exchange process between Br^- in HBr and I^- in SQDs. However, there is only a slight blue-shift of spectra for SQDs-H, so we think there is no introduction of Br^- during the surface cleaning process.

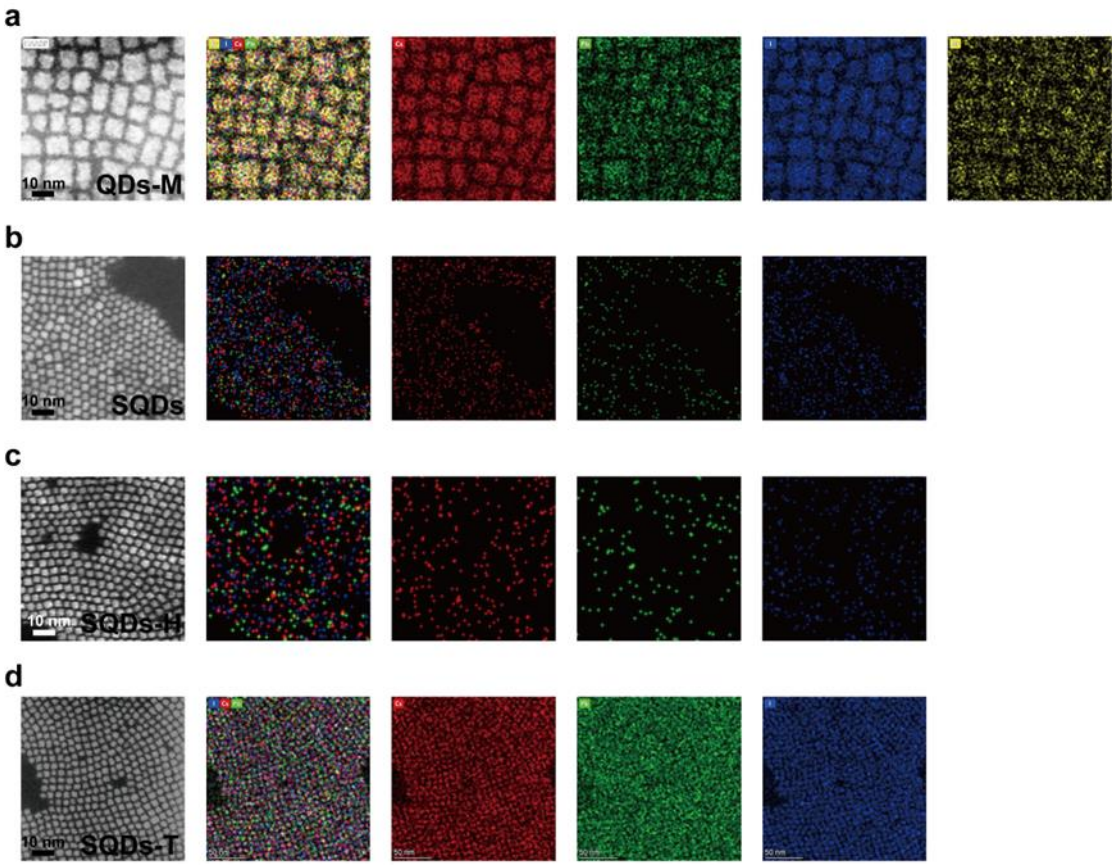

Figure S7. EDS images of **a** QDs-M, **b** SQDs, **c** SQDs-H and **d** SQDs-T, where the ratio of Pb: Br+I in QDs is 1:2.53, in SQDs is 1:2.87, in SQDs-H is 1:3.29, and in SQDs-T is 1: 3.44.

As shown in **Figure S7b-d**, there is no signal of Br^- can be detected for SQDs, SQDs-H and SQDs-T, indicating that Br^- is not introduced into the lattice of $CsPbI_3$ QDs during the surface cleaning process. We observe I/Pb ratios of 2.87 for SQDs, 3.29 for SQDs-H and 3.44 for SQDs-T in Table S1, demonstrating the halide-rich state of SQDs-H after surface-cleaning. The element contents of Cs, Pb, I and Br in specific regions are statistically analyzed during the test. The results show that there is no Br element in SQDs-H and SQDs-T after surface cleaning with HBr. And the 3-PA can effectively bind to bare sites on the SQDs-H surface, further passivating surface defects and improving the stability of QDs. And the EDS confirms that Zn^{2+} cations are not doped into the QDs lattice, because no signal of Zn^{2+} can be found in SQDs, SQDs-H and SQDs-T.

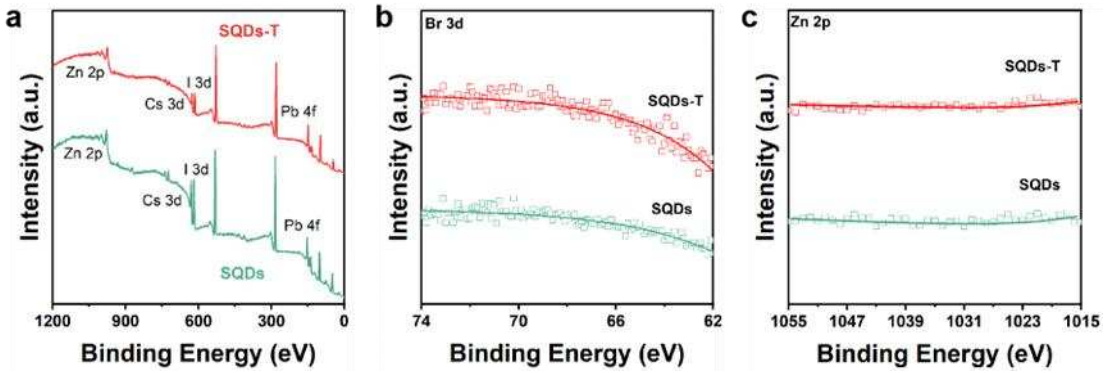

Figure S8. a XPS spectra of SQDs and SQDs-T and **b** high-resolution XPS spectra of Br 3d and **c** high-resolution XPS spectra of Zn 2p of SQDs and SQDs-T.

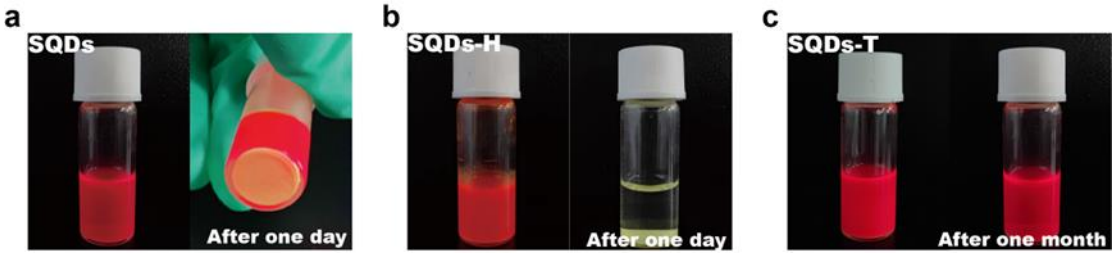

Figure S9. The photographs of **a** SQDs, **b** SQDs-H and **c** SQDs-T preserved in a room temperature environment.

SQDs-H rapidly agglomerate and transfer to the yellow phase after storage for one day, but SQDs-T can retain their colloidal state even after storage for one month. The surface cleaning process reduces the number of defects, but it also removes a large number of surface ligands, resulting in the surface of the SQDs-H being exposed, and high-energy exposed surfaces would cause aggregation and phase transitions of the QDs.

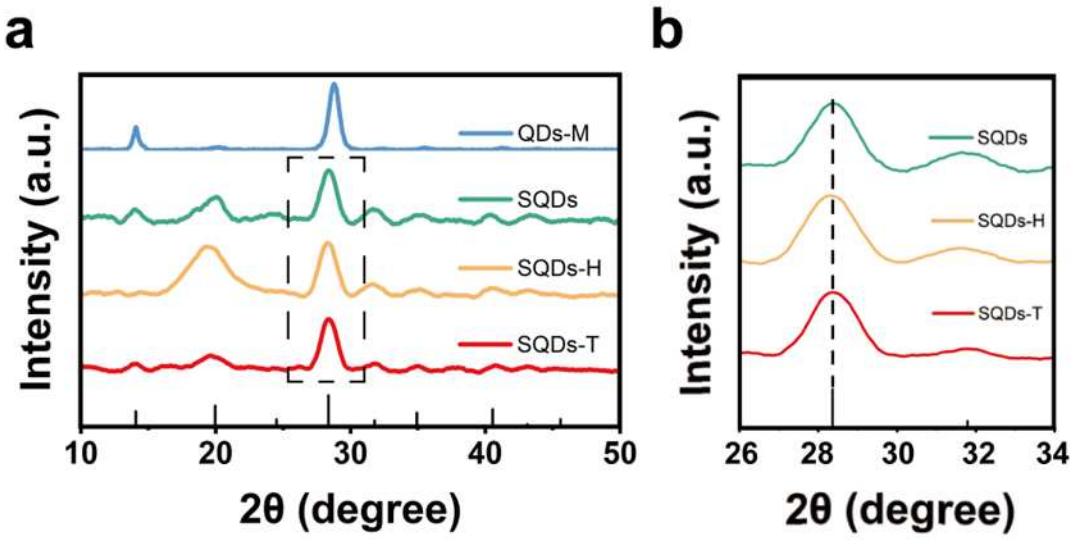

Figure S10. a Comparison of the XRD pattern results of QDs-M, SQDs, SQDs-H and SQDs-T, **b** enlarged-view comparison of the (200) peak position of SQDs, SQDs-H and SQDs-T.

The X-ray diffraction (XRD) pattern of QDs-M shows a narrower linewidth of peak and tendency of shifting to a high angle than that of SQDs, SQDs-H and SQDs-T, indicating the larger size distribution of QDs-M that others and lattice contraction due to the existence of Br in QDs-M (**Figure S10a**). This shift can be attributed to the smaller ionic radius of bromide (Br^-) compared to iodide (I^-). HRTEM images of SQDs, SQDs-H and SQDs-T show the same interplanar distance of 0.628 nm, corresponding to the (100) crystal plane of cubic structure $CsPbI_3$, which is consistent with the XRD pattern results, indicating that the surface cleaning and ligand exchange do not alter the crystal. Also, there are no noticeable peak shifts in the XRD pattern of SQDs-H and SQDs-T compared with that of SQDs (**Figure S10b**), indicating that there is no incorporation of Br^- during the surface-cleaning process. No obvious diffraction peak is observed in SQDs-H near 15°, which may be attributable to the failure of SQDs-H during the observation, resulting in the inconspicuous orientation characteristics of some crystal planes. And XRD results indicate a strong consistent with the standard cubic $CsPbI_3$ phase (PDF#97-016-1481). Furthermore, there are no obviously shifts in the XRD results of SQDs, SQDs-H, and SQDs-T compared to QDs-M. This suggests that the surface-cleaning process does not involve the inclusion of Zn^{2+} ions.

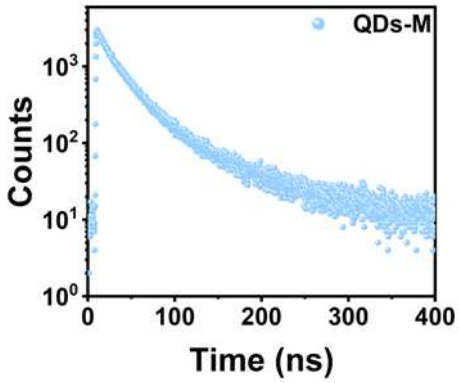

Figure S11. Photoluminescence time-resolved spectra of QDs-M.

QDs-M show a tri-exponential dynamics with a slower radiative rate (K_r) of 1.0×10^{-2} ns^{-1} and a nonradiative rate (K_{nr}) of 1.3×10^{-2} ns^{-1}. It suggests a significant non-radiative channel in the QDs-M.

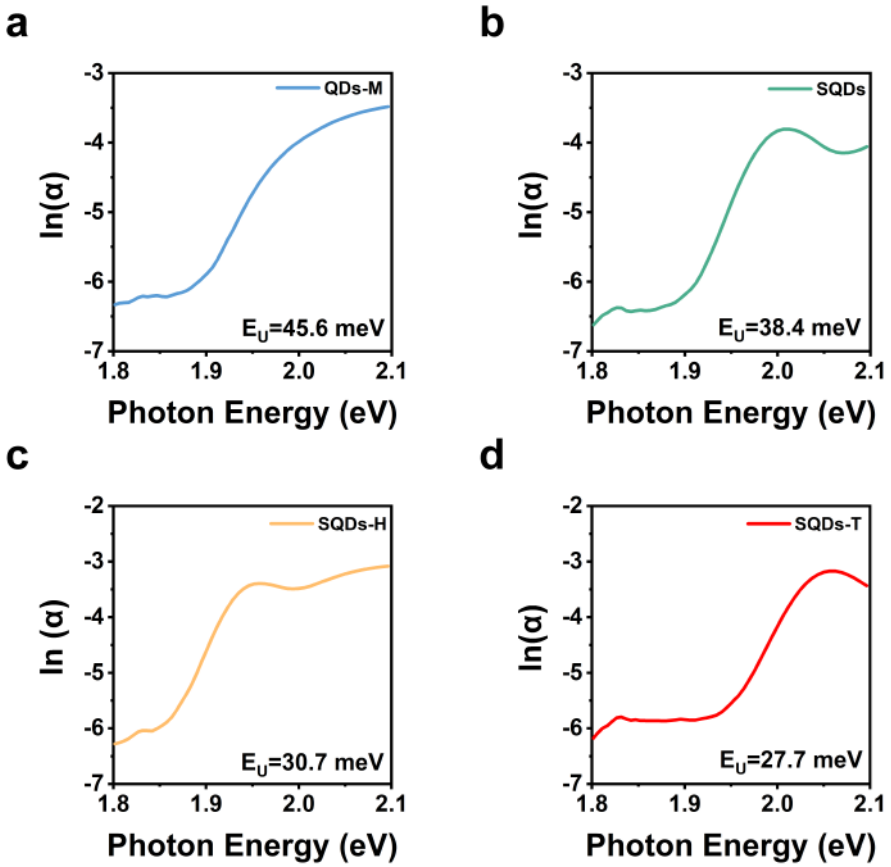

Figure S12. Urbach energies for **a** QDs-M, **b** SQDs, **c** SQDs-H and **d** SQDs-T.

The Urbach energy is generally proportional to trap state density. The smaller Urbach energy of the SQDs-T (27.7 meV) compared to the SQDs (38.4 meV) and SQDs-H (30.7 meV) also indicates low defect density, which is corroborated by the TRPL results.

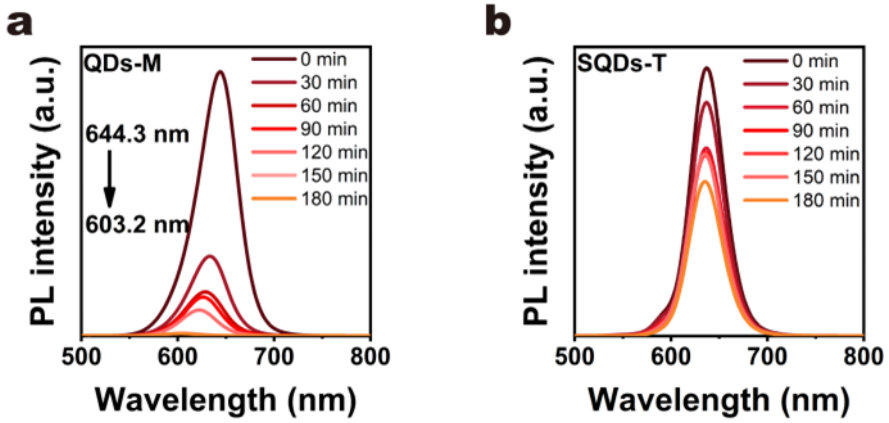

Figure S13. Evolution of PL spectra of **a** QDs-M and **b** SQDs-T under prolonged UV irradiation.

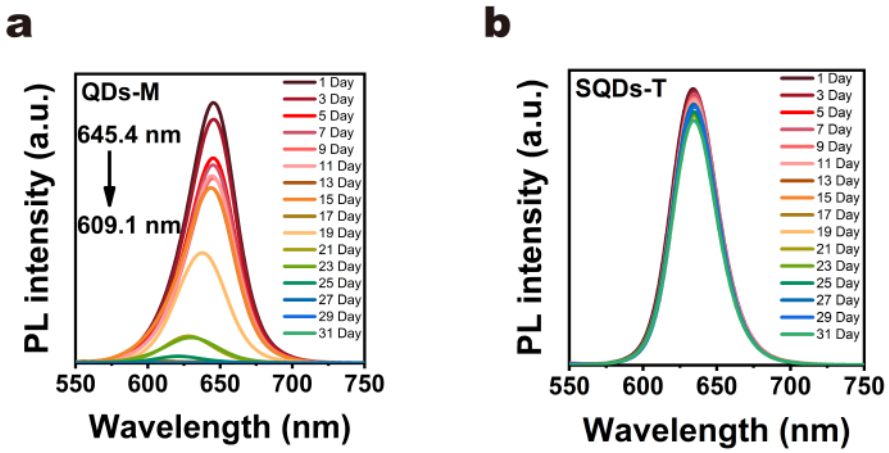

Figure S14. Evolution of PL spectra of **a** QDs-M and **b** SQDs-T under prolonged storage in a room temperature environment.

As shown in **Figure S13**, we monitor the PL peak variation of QDs-M and SQDs-T under continuous ultraviolet (UV, 365 nm wavelength) light irradiation. The PL intensity of the QDs-M decreases significantly with the blue-shifting peak and broadening FWHM, which is attributed to the photo-induced significant migration of halide ions. In contrast, SQDs-T exhibit excellent UV stability, in which FWHM and the peak of the PL spectrum remain almost unchanged under UV exposure for 180 min. The solutions of QDs-M and SQDs-T are continuously monitored under ambient conditions for one month. With the time prolongation, the QDs-M have obviously blue-shifted and show decreasing intensity of the PL spectrum, but the SQDs-T maintain excellent and stable pure-red PL emission at 635 nm (**Figure S14**), indicating that the issue of degradation and spectral stability caused by migration of different halide ions can be settled by this method combining with strongly-confined and surface cleaning-induced ligand exchange.

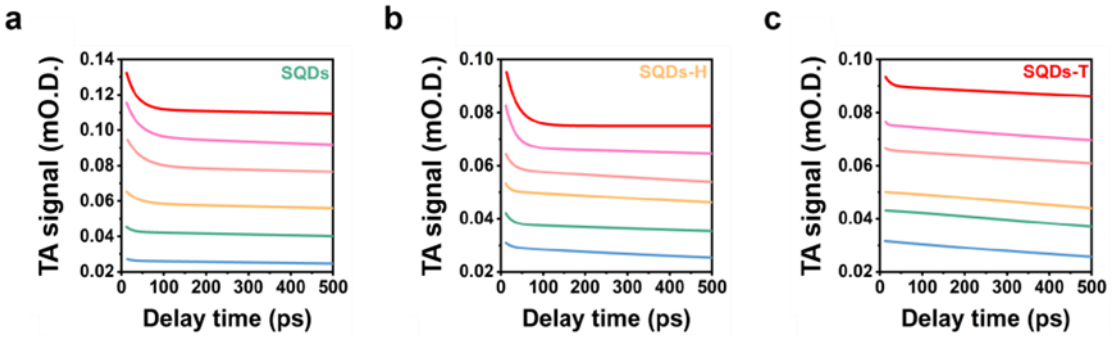

Figure S15. Power dependent kinetic traces of **a** SQDs, **b** SQDs-H and **c** SQDs-T at the exciton bleach (50 μJ/cm^2 - 900 μJ/cm^2).

Electrical excitation of QDs usually has high power density, hence Auger recombination will easily appear during the operational process of PeLEDs and cause efficiency roll-off of devices at high luminance. Obviously, the decay curves of SQDs, SQDs-H, and SQDs-T clearly demonstrate the distinctive decay process under various pump intensities. The decay processes of SQDs and SQDs-H clearly become fast with the gradual increase of the pump intensity. It is evident that when the pump intensity is higher than 200 J/cm^2, SQDs and SQDs-H exhibit a faster decay process than SQDs-T. This finding indicates that SQDs and SQDs-H have experienced significant Auger recombination. However, when the pump intensity is higher than 700 J/cm^2, SQDs-H shows a stronger Auger recombination than SQDs. It is speculated that this is due to the lack of ligand protection on the surface of SQDs-H, which is quenched under a higher power laser. The decay rate of SQDs-T does not change significantly with the pump intensity, indicating that the Auger recombination inside SQDs-T is significantly suppressed.

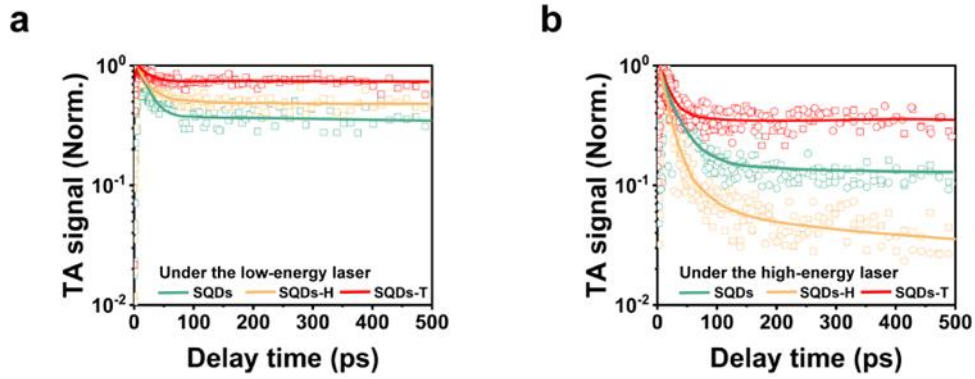

Figure S16. Biexciton recombination kinetics of SQDs, SQDs-H and SQDs-T under **a** the low-energy laser and **b** the high-energy laser.

As the excitation density increases, fast decay components appear on the time scale of several to tens of ps, which is a typical feature of multi-exciton recombination. The biexciton dynamics of SQDs, SQDs-H and SQDs-T are obtained after tests. The lifetime of the corresponding single exciton can be obtained by the double exciton dynamics through the subtraction program. In this figure, we adjust the measured TA trace because we want to set the saturated long-life amplitude to 1. The square and circle of each color are represented by two-by-two subtraction (P2 - P1, P4 - P3, P5 - P4) from the TA kinetics under three different pump intensities (P1, P2, P3, P4, P5; P1 ＜ P2

＜ P3 ＜ P4 ＜ P5). The solid line of each color is the corresponding fitting curve using a single exponential function. The double exciton recombination lifetime (τ) is obtained by the above fitting. Under the low-energy laser (＜ 500 μJ/cm^2) (**Figure S16a**), the Auger rates of SQDs, SQDs-H and SQDs-T decrease in turn, indicating that the Auger recombination is effectively suppressed due to the decrease of defect density, which means that trap-assisted Auger recombination is suppressed. The Auger lifetime of SQDs-T is significantly longer than that of SQDs-H. We speculate that this is because short-chain ligands can effectively inhibit Auger recombination, which will be explained in subsequent texts. Under high-energy laser (＞ 500 μJ/cm^2), SQDs-T show a much longer biexciton lifetime (74.9 ps) compared with SQDs (37.6 ps) and SQDs-H (23.0 ps), indicating the Auger recombination inside SQDs-T is most significantly inhibited (**Figure S16b**). Obviously, SQDs-H show a shorter biexciton lifetime than that of SQDs, which seems contrary to the lower density of traps for SQDs-H, we attribute it to the degradation of SQDs-H surface under high-energy laser due to their bare surface, which instead induces the trap-assisted Auger recombination process. The presence of decreased trap-assisted Auger recombination indicates that 3-PA has the ability to further passivate QD surface sites. The 3-PA has a higher affinity for the surface, resulting in a more effective way to avoid ligand shedding. The Auger recombination inside SQDs-T is significantly inhibited.

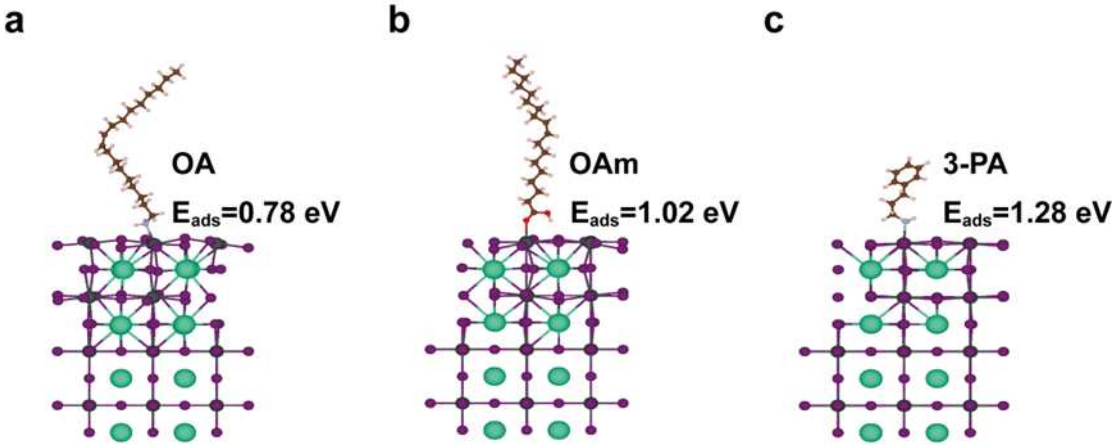

Figure S17. DFT results of the adsorption structures and energies of **a** OA, **b** OAm and **c** 3-PA binding to the surface of QDs.

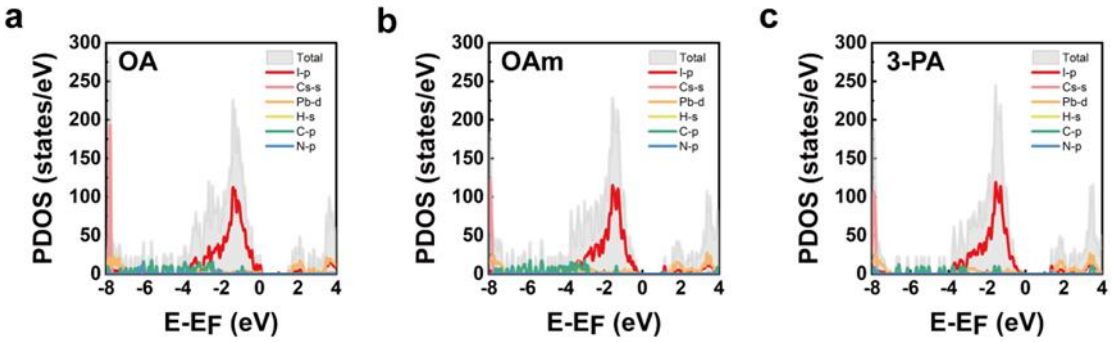

Figure S18. The DFT calculate the density of states (DOS) for QDs with **a** OA, **b** OAm and **c** 3-PA.

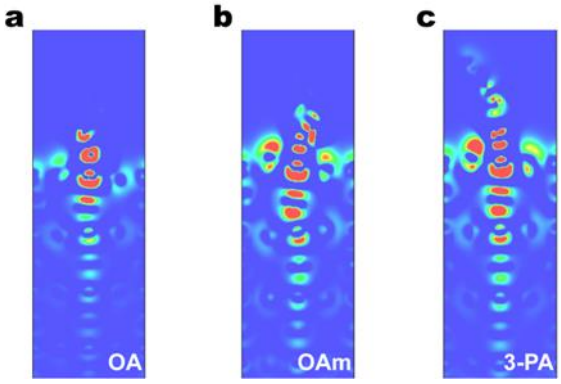

Figure S19. The electronic charge density of QDs with **a** OA, **b** OAm and **c** 3-PA.

First-principles calculations based on the density functional theory (DFT) have been used to clarify the mechanism of the suppressed Auger recombination. We first calculate the absorption energy (E_{ads}) between different types of ligands (OA, OAm and 3-PA) and the QDs surface. The calculations reveal a larger E_{ads} value (1.28 eV) of 3-PA than that of OA (0.78 eV) and OAm (1.02 eV) (**Figure S17**), where the 3-PA exhibits stronger coordination than the initial long-chain ligand. The calculated projected density of states (PDOS) reveals that the QDs without surface-cleaning and ligand exchange exhibit conspicuous trap states near the band edge, i.e. mid-gap states (**Figure**

S18). When the I vacancies of the QDs are removed by surface-cleaning and ligand exchange, the mid-gap states disappear, indicating that the traps have been effectively passivated. The differences between the delocalized charge densities generated by the interaction of the OA, OAm and 3-PA with the surface of QDs can be observed in **Figure S19**. In the surfaces with OA and OAm, the charge density is distributed evenly over all the layers, while on the surface with 3-PA, a significant concentration of charge adjacent to the 3-PA is observed. This observation illustrates that the 3-PA could act as an efficient electron acceptor owing to the strong electronegativity of the benzene ring, attract the charges and concentrate them in the surrounding area, which would alleviate the accumulation of carriers inside QDs and suppress the Auger recombination. These results strongly indicate that the surface of SQDs-T is effectively passivated and the non-radiative Auger recombination is suppressed. Modeling of the electron cloud density at the QDs surface illustrates that the decrease of exciton binding energy is due to the introduction of 3-PA, which affects the electron distribution on the surface of QDs. 3-PA can reversibly store and release electrons driven by local density of redistribution, which enhances the delocalization of electrons in QDs, thereby inhibiting the accumulation of carriers at high carrier concentrations. The above results of the DFT calculations and the temperature-dependent PL spectra indicate that the acceptor action of the benzene ring effectively decreases E_B and inhibits Auger recombination.

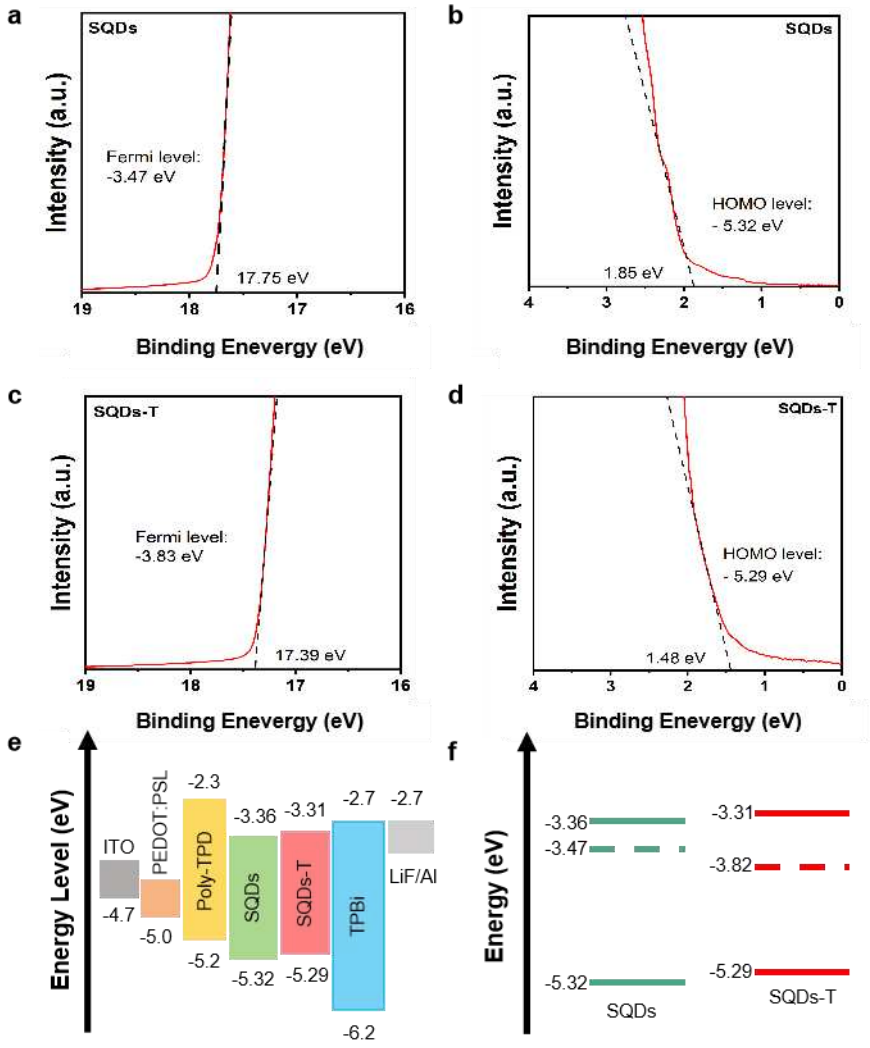

Figure S20 The Fermi level and HOMO level of **a, c** SQDs and **b, d** SQDs-T; **e** energy level diagram of SQDs and SQDs-T used in PeLEDs; **f** the energy level diagram of SQDs and SQDs-T based on UPS results.

For the SQDs, the Fermi level and conduction band minimum (CBM) are determined as -3.47 and -3.36 eV, respectively, identifying a heavily doped n-type behavior. For the SQDs-T, the Fermi level (-3.82 eV) shifts away from the CBM (-3.31 eV), identifying a nearly ambipolar behavior. SQDs-T also induce a 0.03 eV upshift of the valence band maximum (VBM) along with the switching from n-type behavior to nearly ambipolar. They together will promote the hole injection, thus a suppressed efficiency roll-off.

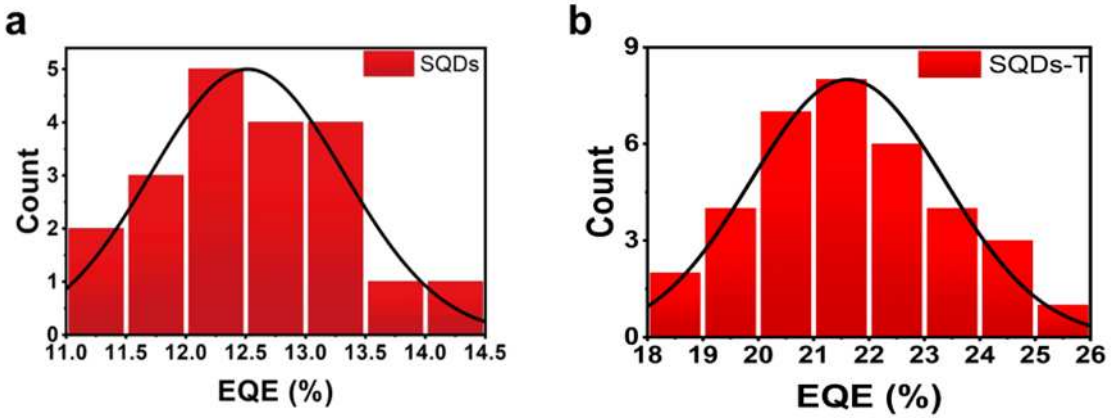

Figure S21. Histograms of EQE of PeLEDs fabricate with **a** SQDs and **b** SQDs-T.

The average peak EQE (counting 50 devices) of PeLEDs with SQDs-T (22.0%) is higher than that of SQDs PeLEDs (12.5%), manifesting good reproducibility of the device performances.

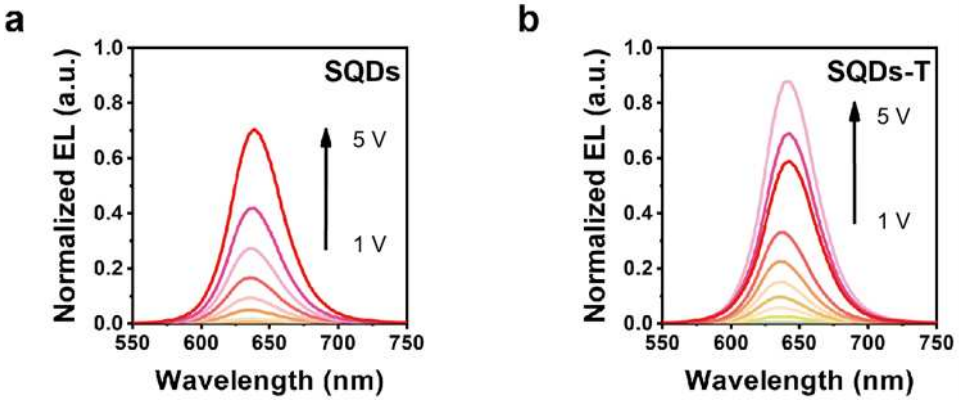

Figure S22. EL spectra of devices prepare using **a** SQDs and **b** SQDs-T at different operational voltages.

Spectral and operational stability are key factors for the application of PeLEDs. Notably, the EL peak of SQDs-T PeLEDs exhibits excellent spectral stability during device operation, with a slight red-shift of the EL spectra even at a high voltage of 5 V, which is caused by current-induced Joule heating.

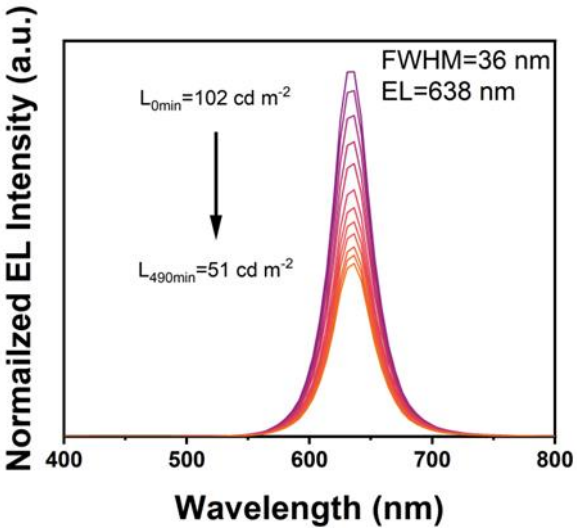

Figure S23. Evolutions of EL spectra during the measurement of operational half-lifetime T_{50}.

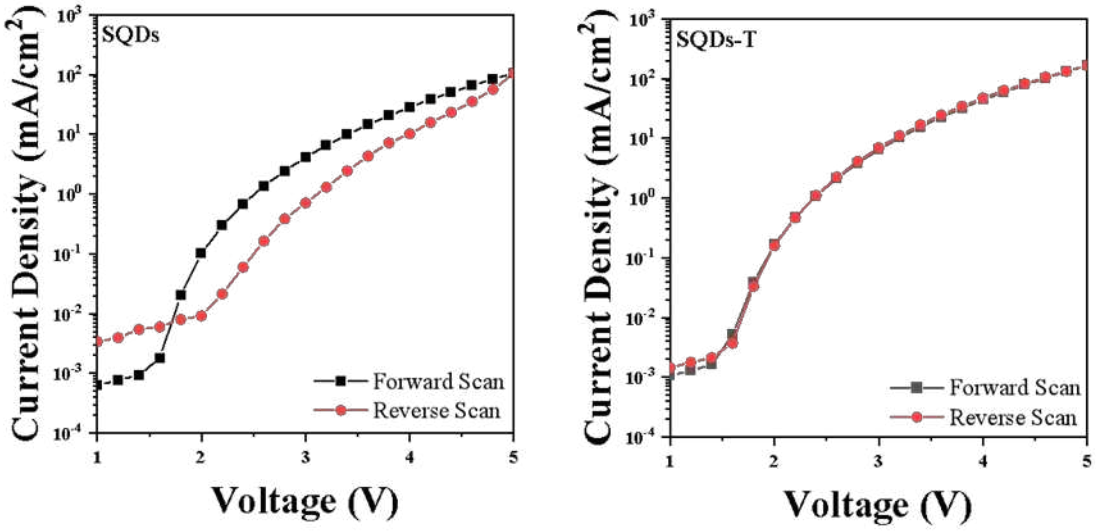

Figure S24. The investigation of hysteresis in SQDs-based LED and SQDs-T-based LED.

The LED based on SQDs does exhibits hysteresis when comparing forward and reverse scans. However, SQDs-T LEDs demonstrate a comparatively lower level of hysteresis, suggesting that the SQDs-T have low trap states and effectively suppress ion migration.

Table S1. The concentration of different elements in QDs-M, SQDs, SQDs-H and SQDs-T is calculated from the EDS mapping.

Sample Code	Element	Atomic Fraction (%)	Pb: Br+I
QDs-M	Cs	23.75	1:2.53
	Pb	21.56	
	Br	17.11	
	I	37.58	
SQDs	Cs	19.75	1:2.87
	Pb	20.73	
	Zn	0	
	Br	0	
	I	59.52	
SQDs-H	Cs	17.69	1:3.29
	Pb	19.17	
	Zn	0	
	Br	0	
	I	63.14	
SQDs-T	Cs	18.54	1:3.44
	Pb	18.31	
	Zn	0	
	Br	0	
	I	63.15	

Table S2. Summary of time-resolved PL fitting parameters for solutions of QDs-M, SQDs, SQDs-H and SQDs-T solutions.

Sample Code	f_1 [%]	τ_1 [ns]	f_2 [%]	τ_2 [ns]	f_3 [%]	τ_3 [ns]	τ_{ave} [ns]	PLQY [%]	$K_r \times 10^{-2}$ [ns^{-1}]	$K_{nr} \times 10^{-2}$ [ns^{-1}]
QDs-M	12.9	10.6	62.1	27.8	25.0	97.3	43.0	45	1.0	1.3
SQDs	81.5	12.1	18.5	15.1			12.6	78	6.2	1.74
SQDs-H	100	14.9					14.9	95	6.4	0.3
SQDs-T	100	15.3					15.3	99	6.5	0.06

The SQDs-T show the slowest non-radiative rate (6×10^{-4} ns^{-1}) compares to those of SQDs (1.74×10^{-2} ns^{-1}) and SQDs-H (3×10^{-3} ns^{-1}). These results serve as compelling evidence of the significantly reduced nonradiative rate by surface-cleaning and ligand exchange. By performing further ligand exchange, the surface dangling bonds and bare sites may be further passivated, resulting in a significant decrease in non-radiative recombination caused by defect states. This reduction in non-radiative recombination correlates with the very high PLQY achieved in the SQDs-T.

Table S3. Summary of TA spectra fitting parameters for solutions of SQDs, SQDs-H and SQDs-T under the pulse energy density of 50 μJ/cm^2.

Sample Code	f_1 **[%]**	τ_1 **[ps]**	f_2 **[%]**	τ_2 **[ps]**
SQDs	100	821.5	-	-
SQDs-H	100	1678.1	-	-
SQDs-T	100	4061.1	-	-

Table S4. Summary of TA spectra fitting parameters for solutions of SQDs, SQDs-H and SQDs-T under the pulse energy density of 900 μJ/cm^2.

Sample Code	f_1 **[%]**	τ_1 **[ps]**	f_2 **[%]**	τ_2 **[ps]**
SQDs	13.2	23.1	86.8	1181.9
SQDs-H	4.8	15.1	94.2	1223.5
SQDs-T	1.01	58.1	98.9	2235.5

Table S5. Summary of the performance of a typical PeLEDs device with pure-red emission.

Materials	EL Peak [nm]	Max. Luminance [cd/m^2]	Max. EQE [%]	Operational lifetime [min]	Ref.
$CsPbI_3$ QDs	653	800	18	87	1
HPAI-TBSI-$CsPbI_3$ QDs	630	1212	6.4	32	2
NH_4I-$CsPbI_3$ QDs	645	523	9.4	25.1	3
$CsPbI_3$ NCs	620	13644	6.2	13.5	4
$MAPb(I_xBr_{1-x})_3$ NCs	620	627	20.3	-	5
$CsPbI_{3-x}Br_x$ QDs	637	2653	21.8	70	6
In^{3+} doped-$CsPbBr_xI_{3-x}$ QDs	639	423	11.2	-	7
TRP-$CsPbI_{3-x}Br_x$ NCs	635	12910	22.8	63	8
BS-$CsPbBr_xI_{3-x}$ NCs	638	1515	23.5	97	9
$CsPbI_3$ QDs	636	3775	20.8	7.4	10
$PbCl_x$-$CsPbI_3$ QDs	638	2511	26.1	450	11
$CsPbI_3$ QDs	638	18500	26.0	490	This work

References

1. Chen, D. et al. Amino Acid-passivated pure red $CsPbI_3$ quantum dot LEDs. *ACS Energy Lett.* **8**, 410-416 (2022).
2. Lan, Y. F. et al. Spectrally stable and efficient pure red $CsPbI_3$ quantum dot light-emitting diodes enabled by sequential ligand post-treatment strategy. *Nano Lett.* **21,** 8756-8763 (2021).
3. Shen, W.et al. Spectrally stable pure red $CsPbI_3$ quantum dots light-emitting diodes via effective low temperature gradient centrifugation separation and surface modification. *Adv. Opt. Mater.* **5**, 2300306 (2023).
4. Bi, C et al. Self-assembled perovskite nanowire clusters for high luminance red light-emitting diodes. *Adv. Funct. Mater.* **30**, 2005990 (2020).
5. Hassan, Y. et al. Ligand-engineered bandgap stability in mixed-halide perovskite LEDs. *Nature* **591**, 72-77 (2021).
6. Xie, M et al. Suppressing ion migration of mixed-halide perovskite quantum dots for high

efficiency pure-red light-emitting diodes. *Adv. Funct. Mater.* **4**, 2300116 (2023).

7. Zhou, X. et al. Near-unity quantum yield and superior stable indium-doped $CsPbBr_xI_{3-x}$ perovskite quantum dots for pure red light-emitting diodes. *Adv. Opt. Mater.* **10,** 2101517 (2022).
8. Zhang, J. et al. Ligand-induced cation-Π interactions enable high-efficiency, bright and spectrally stable Rec. 2020 pure-red perovskite light-emitting diodes. *Adv. Mater.* **35**, 2303938 (2023).
9. Zhang, J. et al. A multifunctional "halide-equivalent" anion enabling efficient $CsPb(Br/I)_3$ nanocrystals pure-red light-emitting diodes with external quantum efficiency exceeding 23%. *Adv. Mater.* **35**, 2209002 (2023).
10. Xie, M. et al. High-efficiency pure-red perovskite quantum-dot light-emitting diodes. *Nano Lett.* **22**, 8266-8273 (2022).
11. Feng, Y.et al. Nucleophilic reaction-enabled chloride modification on $CsPbI_3$ quantum dots for pure red light-emitting diodes with efficiency exceeding 26%. *Angew. Chem. Int. Ed.* **63**, 202318777 (2024).